RSC Advances

ROYAL SOCIETY OF CHEMISTRY

www.rsc.org/advances

In situ calcium phosphates deposition in hydrogels of poly(acrylic acid)-polyacrylamide interpenetrating polymer networks

M. M. Simeonov, A. A. Apostolov and E. D. Vassileva

ABSTRACT

Interpenetrating networks of poly(acrylic acid) and polyacrylamide were used for the first time as templates for *in situ* calcium phosphates (CP) deposition in an attempt to mimic the natural occurring biomineralization. The process of CP deposition was controlled by two main factors: the functionality and the overall crosslinking density of the IPNs' gels, both factors being varied via the IPNs' composition. The approach allowed to control the CP deposition in terms of amount, type and crystallite size. In this way the IPNs' potential as a template for controlled biomineralization was demonstrated. The obtained new inorganic-organic composite materials were characterized and their further potential in the field of bone regeneration and substitution was revealed.

1. Introduction

Biomineralization in nature is guided by anionic proteins, which regulate and control the process of mineral deposition. For example, mollusks build their shells by using a hydrophobic silk gel, *aspartic acid rich proteins*, and an amorphous precursor phase from which the calcium carbonate crystals form [1]. Natural bone consists of a collagen I fibrils matrix on which carbonated apatite is deposited. The deposition process is promoted by *anionic proteins* which serve as nucleating agents, the anionic groups' concentration in the guiding proteins depending on the bone's type and age [2].

Following the nature's lessons, the incorporation of anionic groups onto a polymer backbone became a common approach for polymer scaffolds mineralization [2, 3]. The crystal growth in gels has emerged as a popular platform for biomineralization processes, the interest being further enhanced by the growing number of gel-like matrices identified to play key role in the mineralization performed by biological organisms [4]. The gel chemical *functionality* defines the way the gel interacts with solutes and thus either suppresses or enhances nucleation [5, 6]. On the one hand, when the gel functionality acts as heterogeneous nuclei, higher nucleation densities will be observed within the gels than in solution. On the other hand, the nucleation in gels, due to the diffusion-limited supply of reactants, takes place only when solutes accumulate to higher supersaturation than in solution. Thus besides the functionality, the

crosslinking density of gels is another tool to influence the *in situ* crystal growth. In this way, in gels a controllable number of heterogeneous nuclei are formed but the probability for these nuclei to reach the critical size required for growth is reduced. Usually, gels yield *smaller number of crystals* with *larger sizes* compared to the solution-grown crystals [4].

In general, the crystal growth in hydrogels becomes an alternative to solution-based strategies as it provides different ways to control the mineral crystallization, e.g. *the rate of nucleation, the number and the size of crystals, their morphology*, etc.

Calcium phosphate based materials are widely used for bone augmentation and restoration. Brushite (dicalcium phosphate dihydrate, DCPD, $CaHPO_4.2H_2O$) and monetite (dicalcium phosphate anhydrous, DCPA, $CaHPO_4$) are of considerable interest in this respect due to their metastable nature in body fluids [7]. Both exhibit the ability to be resorbed under physiological conditions and their resorptive capacity and solubility defines their osteoconductive and osteoinductive properties [8]. The interest towards such kind of materials is increasing in recent years as they quickly resorb in the body and give rise to a newly regenerated bone tissue [9].

Interpenetrating polymer networks (IPNs) are combination of two or more polymer networks which are not covalently bonded but penetrate into each other [10]. In order to separate them one need to break covalent bonds. This fact lies behind their very efficient energy absorbing ability which defines e.g. the IPNs excellent damping properties. When obtained via the sequential method, IPNs are characterized by a phase separated morphology where the 1^{st} network acts as a matrix within which nodules from the 2^{nd} one are finely dispersed (Scheme 1). When the 1^{st} network is densely crosslinked the nodules from the 2^{nd} network are nanosized, i.e., a nanophase separated structure could be formed. With increasing the ratio of the 2^{nd} to the 1^{st} network, the nodules from the 2^{nd} network start to touch each other and the nodular morphology is transformed into an inter-connected nodular structure [10]. In this way an inversing of the phases could occur. This specific and controllable by the IPNs composition only nanophase separated structure could be utilized for guiding the biomineralization processes – an approach which is novel and not explored until now.

The aim of this study was to exploit the potential of IPNs as hydrogel media for crystal growth and to demonstrate that the proper selection of IPNs components (functionality) as well as the IPN composition (network density and nanostructure) are powerful tools for controlling the *in situ* mineralization process. This novel approach was demonstrated by utilizing the IPNs of PAA and PAAm as templates for biomimetic mineralization.

2. Experimental Section

2.1. Materials

Acrylamide (AAm, purum, >=98.0%) was purchased from Fluka AG, Germany. Acrylic acid (AA, anhydrous, 99%) was purchased from Across Organics, Belgium. Potassium peroxodisulfate (PPS) and N,N'-methylenebisacrylamide (MBAA) were purchased from Sigma-Aldrich. Potassium hydrogen phosphate, K_2HPO_4 (anhydrous) was purchased from Merck, Germany and calcium chloride $CaCl_2$ (anhydrous) was purchased from Sigma-Aldrich. All reagents were used as received without further purification.

2.2. IPNs synthesis

The IPNs of poly(acrylic acid) PAA and polyacrylamide (PAAm) were synthesized via the sequential method. Two types of IPNs were obtained, differing in the order of formation of both networks, respectively IPNs PAAm/PAA and IPNs PAA/PAAm (Scheme 1).

2.2.1. IPNs PAAm/PAA

At the first step of IPNs PAAm/PAA formation, PAAm single network (SN) was prepared as described previously [11]. Briefly, a free radical crosslinking polymerization of acrylamide (1.14M aqueous solution), 0.1 wt. % PPS and 4 wt. % MBAA, both % relatively to the monomer weight, was performed at 60˚C for 5 hours. PAAm SNs were washed in distilled water to completely remove traces from non-reacted chemicals (followed by UV of the waste waters). The AAm conversion to PAAm network was determined to be 99%±1% via UV as described elsewhere [12].

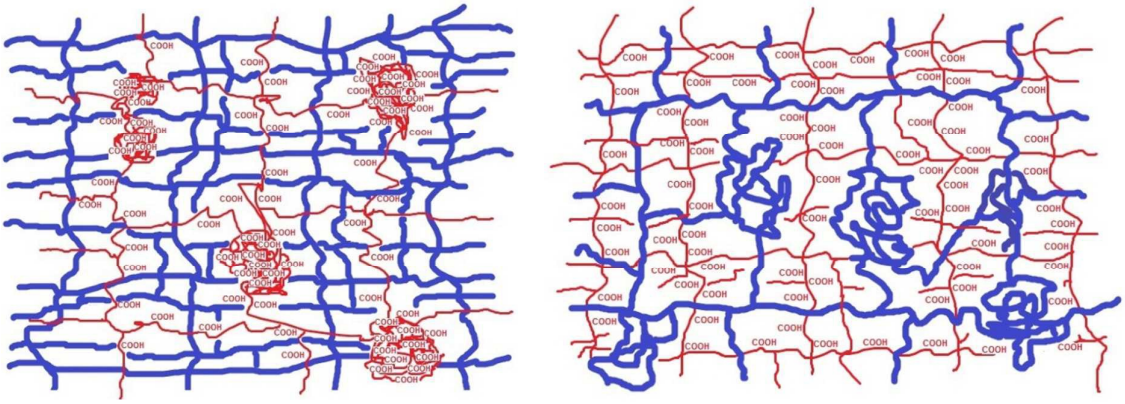

IPN PAAm/PAA **IPN PAA/PAAm**

Scheme 1. Schematic presentation of the IPNs of (A) PAAm/PAA and (B) PAA/PAAm.

At the next step five PAAm SNs were left to swell in acrylic acid (AA) aqueous solutions with concentrations 1M, 2M, 3M, 4M, and 5M, respectively, containing also 0.1 wt.% PPS and 4 wt. % MBAA (both % relatively to AA). The *in situ* crosslinking polymerization of

acrylic acid into SN PAAm took place at 60˚C for 5 hours. In this way five IPNs with different PAAm/PAA ratio were obtained (Table 1). Each of the newly synthesized IPNs PAAm/PAA was washed in distilled water to completely remove traces from non-reacted chemicals. The AA conversion to PAA network was determined to be 98%±1% by titration with NaOH of the waste waters from the washing procedure.

2.1.2. IPNs PAA/PAAm

IPNs PAA/PAAm were prepared as described previously [11] by exchanging the order of formation of PAAm and PAA networks (Scheme 1). At the first stage PAA SNs were synthesized by using 1.14M AA aqueous solution, containing 0.1 wt.% PPS and 4 wt. % MBAA. The crosslinking polymerization conditions and washing procedure were the same as already described above. Then SNs PAA were left to swell into AAm aqueous solutions with concentrations from 1M to 5M, containing also 0.1 wt.% PPS and 0.1 wt. % MBAA (both % relative to AA). The *in situ* crosslinking polymerization conditions and washing were the same as described for the IPN PAAm/PAA.

For both synthetic procedures, high concentration of the crosslinking agent MBAA (4 mol.%) was used as a way to decrease the size of the 2nd network domains, i.e. to attain nano dimension of the phase separated IPNs' structure.

Following these two synthetic procedures, five PAA/PAAm and five PAAm/PAA IPNs with different ratio between both components were obtained (Table 1). For sake of comparison one SN PAA and one SN PAAm were used as referent samples.

Table 1. Sample designation of IPNs and SNs in terms of φ^{PAA}.

Sample desig-nation	SN PAAm	IPN PAA/PAAm					IPN PAAm/PAA					SN PAA
		IPN1	IPN2	IPN3	IPN4	IPN5	IPN6	IPN7	IPN8	IPN9	IPN 10	
φ^{PAA}	0	0.20	0.24	0.26	0.32	0.45	0.52	0.64	0.65	0.68	0.69	1

Table 1 summarizes all prepared SNs and IPNs and each network is designated in terms of its PAA weight fraction determined by the equation:

$$\varphi^{PAA} = \frac{m^{PAA}}{m^{PAA}+m^{PAAm}} \qquad (1)$$

where m^{PAA} and m^{PAAm} are respectively the weights of the PAA and PAAm in the IPNs, while φ^{PAA} is the weight fraction of PAA in the IPNs. m^{PAA} for each sample was determined from the titration of the non-reacted AA, while m^{PAAm} was determined by applying the UV method as mentioned above.

2.1.3. *In situ* calcium phosphates (CP) precipitation in IPNs

Dry disks from the IPN samples with diameter 6 mm and thickness 1 mm were swollen in 0.3M $CaCl_2$ aqueous solution. After reaching constant weight, the samples were washed with distilled water and transferred into 0.5 M K_2HPO_4. The procedure is illustrated in Scheme 2.

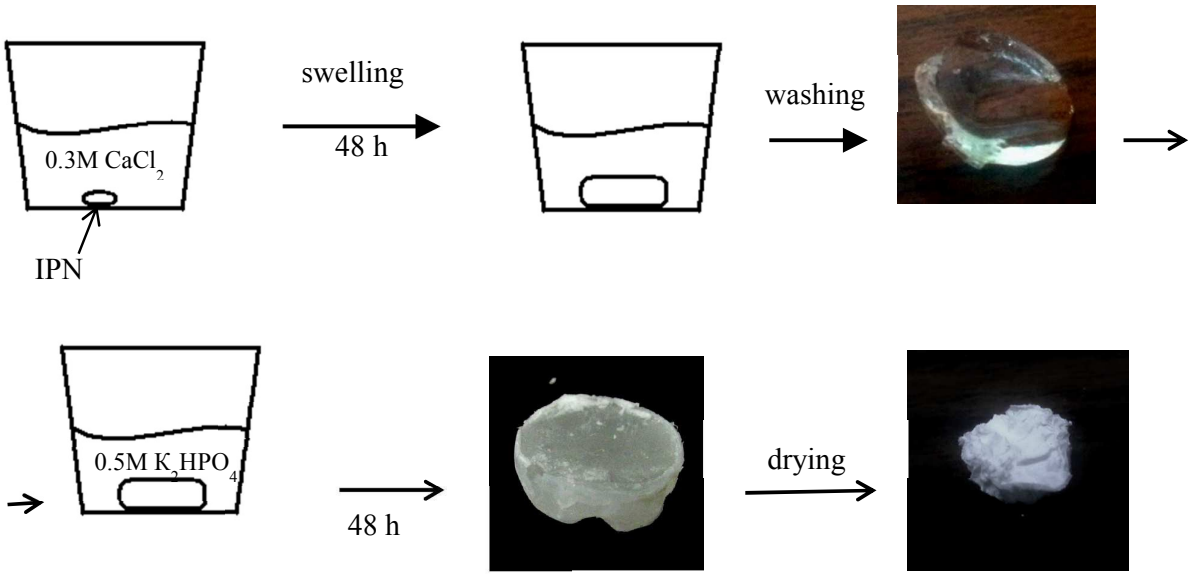

Scheme 2. Procedure of the *in situ* calcium phosphates (CP) formation in IPNs.

The amount of the *in situ* formed CP (w^{CP}) was determined gravimetrically after washing out for 24 h in distilled water the inorganic salts (e.g. KCl), formed as side products from the CP precipitation:

$$w^{CP}\% = \frac{w_{IPN}^{CP} - w_{IPN}}{w_{IPN}^{CP}} .100 \qquad (2)$$

where w_{IPN} is the weight of dry IPNs without CP and w_{IPN}^{CP} is the weight of dry IPNs after CP *in situ* formation.

The successful washing was checked via scanning electron microscopy (SEM) using energy dispersive spectroscopy (EDS) analysis, the results are presented in the Supporting Information (Figure S1).

2.3. IPNs' characterization

2.3.1. Equilibrium swelling ratio (ESR) of IPNs

Dry disk shaped pieces with diameter 6 mm were cut from IPN films with different composition and each piece was weighted. Then the pieces were swollen in distilled water until reaching a constant weight and their ESRs were determined following the equation:

$$ESR = \frac{m_{swollen} - m_{dry}}{m_{dry}} \qquad (3)$$

Here, $m_{swollen}$ and m_{dry} are respectively the weights of the swollen and the dry piece. The final ESR value for each IPN was obtained after averaging the results for at least 12 pieces.

2.3.2. Microhardness

The microhardness of the neat IPNs and SNs was tested with an apparatus for Vickers microhardness measurements (Leica VMHT, Leica Mikrosysteme GmbH, Wien, Austria) at three different loads: 500, 1000 and 2000 gf and indentation time 16 s. At each load, 5 indentations were made and the results obtained for both diagonals of the indentation marks were averaged. From the slope of the $P = f(d^2)$ dependence, where P is the load in N and d is the diagonal in mm, the Vickers microhardness value (HV) in MPa was determined, using the equation:

$$HV = 1.854\frac{P}{d^2} \qquad (4)$$

Here, 1.854 is a constant, reflecting the geometry of the pyramidal diamond indenter used for the Vickers hardness measurements.

2.3.3. Differential scanning calorimetry (DSC)

Differential scanning calorimetry tests were performed on DSC Q200 apparatus by TA Instruments, USA. Dry samples were heated from 30 to 230˚C with 10˚C/min heating rate under nitrogen flow (50 mL/min).

2.3.4. ATR Infrared spectroscopy (IR)

IR spectra of IPNs with *in situ* formed CP were obtained in regime of reflectance by using IRAffinity-1 Shimadzu Fourier Transform Infrared (FTIR) spectrophotometer with MIRacle Attenuated Total Reflectance Attachment.

2.3.5. X-ray diffraction (XRD)

A Siemens D500 diffractometer, Germany, with secondary monochromator and Cu-Kα radiation was used to obtain the diffractograms over 2θ range of 10-80^o with a step of 0.03^o and count time of 10 s. The search-match program Match2 was used to identify the phases [13]. The crystallite size D_{hkl} (in Å) in direction perpendicular to the (hkl) plane was calculated according to Scherrer's formula [14]:

$$D_{<12\bar{1}>} = \frac{1{,}07.\lambda}{\beta_{1/2}\cos\theta} \qquad (5)$$

where λ=1.542 Å is the wavelength used, 2θ is the reflection position and $\beta_{1/2}$ in rad is the physical integral width of the reflection hkl positioned at 2θ. Gaussian function was used to approximate the reflections. $\beta_{1/2}$ was obtained from the experimental width B and instrumental width b [15]:

$$\beta^2 = B^2 - b^2 \qquad (6)$$

where b was measured from the diffractogram of annealed standard of SiO_2 (PDF # 83-2465) expressing reflection 100 at 20.9 deg 2θ.

2.3.6. Scanning electron microscopy (SEM)

The morphology of fractured surface of IPNs (with in situ deposited CPs) with various composition, was examined by scanning electron microscope JSM-5510, JEOL, Japan, operating at 10 kV. The samples were prepared for imaging by coating with gold for 30 s using a sputter-coater JSC 1200, JEOL, Japan, under argon atmosphere.

3. Results and discussion

3.1. Swelling properties

ESR dependence on PAA weight fraction (φ^{PAA}) is presented in Figure 1 for both types of IPNs. It starts with drop of ESR at low φ^{PAA} as compared to the ESR of SN PAAm (IPN PAA/PAAm, solid symbols in Figure 1). Similar drop at low φ^{PAA}<0.26 was already observed for IPN PAA/PAAm with similar composition in our previous work [11]. It was explained by the entanglement of PAA and PAAm networks in the IPNs and as these entanglements act as physical junctions, it is expected that the ESR of the IPNs would decrease when compared to the neat PAAm.

The further PAA weight ratio increase (φ^{PAA}>0.26) results into a IPNs' ESR increase which tends to the ESR of the neat PAA (Figure 1). This behaviour is explained by the PAA ionization, which is high in distilled water (pK_a^{PAA}=4.5). For example at pH=7 about 70% of the PAA carboxylic groups are ionized [16]. Thus, in the IPNs swollen state most of the acid groups in PAA are transformed into carboxylic anions [17]. It is known that when PAA and PAAm are mixed to form an interpolymer complex, in fact PAA dictates the configuration of the complex [18]. When φ^{PAA} increases, the contribution of the PAA to the overall behavior of the IPNs also increases. Due to the repulsion between COO^-, the PAA network is stretched and hence the IPNs' ESR increases. As a result, at high PAA content, the IPNs' ESRs approach the ESR of SN PAA network.

In summary, when the PAA content in the IPNs increases, the repulsive interactions also increase due to the higher number of carboxylic anions that results into more extended PAA network, respectively into higher swelling ability of the IPNs and higher ESR values.

At lower PAA content (φ^{PAA}<0.26), although the PAA carboxylic groups are ionized, their amount is too low to influence significantly the behavior of the whole IPN. The repulsive interactions between carboxylic anions of PAA are shielded by the PAAm chains which

significantly prevail in number. Thus at low φ^{PAA} (IPN1 and IPN2), the ESR dependence on IPN composition is guided not by the PAA ionization but rather by the entanglements between PAA and PAAm chains.

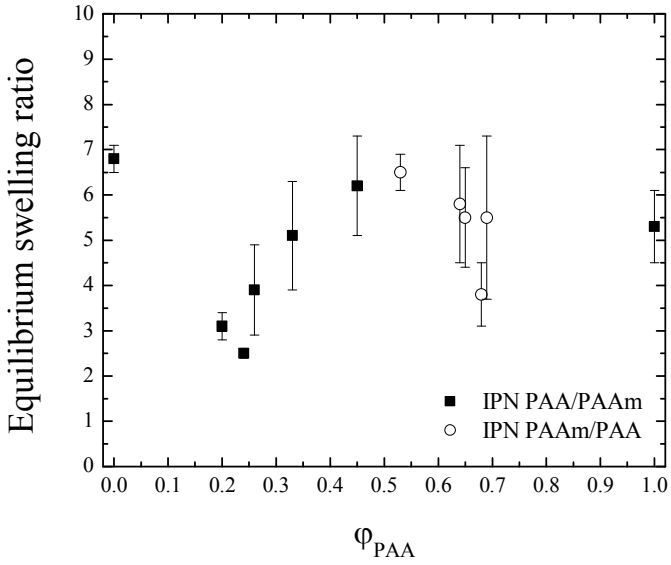

Figure 1. Equilibrium swelling ratios for both types of IPNs vs. IPN composition.

One should mention here, that PAA and PAAm could form H-bonds between themselves when PAA is at low ionization degree (pH<4.5). Then PAA could form either intramolecular or intermolecular H-bonds with itself as well as with PAAm. This happens also in solid state where the interpolymer complexation between PAA and PAAm is very strong [18]. At neutral pH, the H-bonding could also occur but is less probable due to the PAA ionization.

3.2. Microhardness (MH)

In Figure 2 the MH values of the IPNs are presented as a function of φ^{PAA} as well as the MH of both SNs PAA and PAAm. There is no clear trend for the MH dependence on the IPNs' composition. It should be however pointed out that the MH values of IPNs are higher as compared to the MH of both SNs as well as higher to the predicted values from the additivity law (solid line in Figure 2). This confirms the mutual interlacing, i.e. the formation of additional physical junctions, between both networks PAA and PAAm in IPNs assumed above (Figure 1). This positive deviation from the additive law reflects also the already mentioned strong propensity for interpolymer complexation and H bonding between PAA and PAAm in solid state where MH was measured.

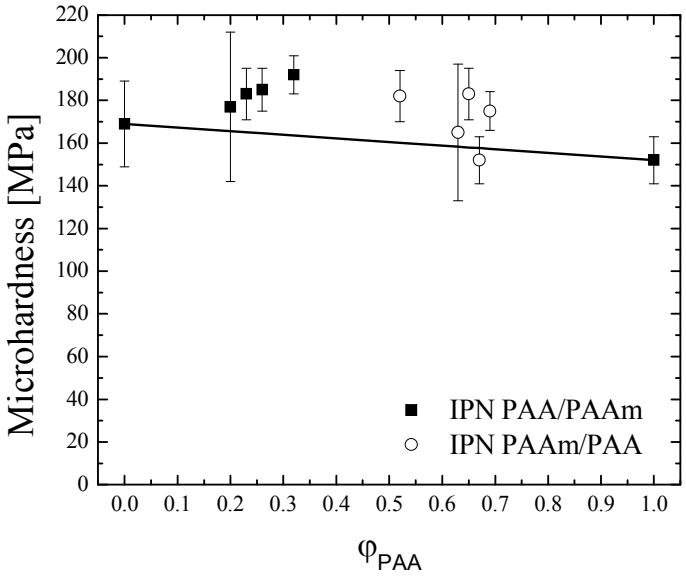

Figure 2. Microhardness vs. IPNs' composition. Solid line is drawn according to the additivity law.

3.3. Thermal properties of IPNs

In Figure 3 the DSC thermograms of IPNs PAAm/PAA as well as for both SNs PAA and PAAm are presented. For SN PAAm ((φ^{PAA}=0, Figure 3) an endothermic peak at ~220°C appears which is known to be due to the 1st stage of PAAm thermal decomposition. It takes place in the range of 220 to 330°C and consists in reaction of imidization between the PAAm amino groups which results into an NH_3 release [19]. SN PAA is also known to have a decomposition peak at 230°C, but in the neat PAA thermogram it could not be seen (φ^{PAA}=1, Figure 3).

The onset of the PAAm degradation peak is observed for all IPNs compositions. When compared to the neat PAAm, this onset is shifted to higher temperatures, which means that the IPN formation increases the PAAm thermal stability. This thermal stability improvement of IPNs could be explained by the shielding effect that the PAA chains have on the PAAm chains, separating the amino groups and not allowing them to take part in the imidization reaction. This explanation is supported by the fact that the peak corresponding to the 1st stage of the thermal degradation of PAAm in IPNs shifts to lower temperatures as PAAm content increases. That means that as the decomposing component (PAAm) content increases, more and more PAAm chains are coming closer to each other, thus enhancing the imidization

reaction. In summary, the IPNs of PAA and PAAm possess higher thermal stability when compared to the neat PAAm and their thermal stability is composition dependent.

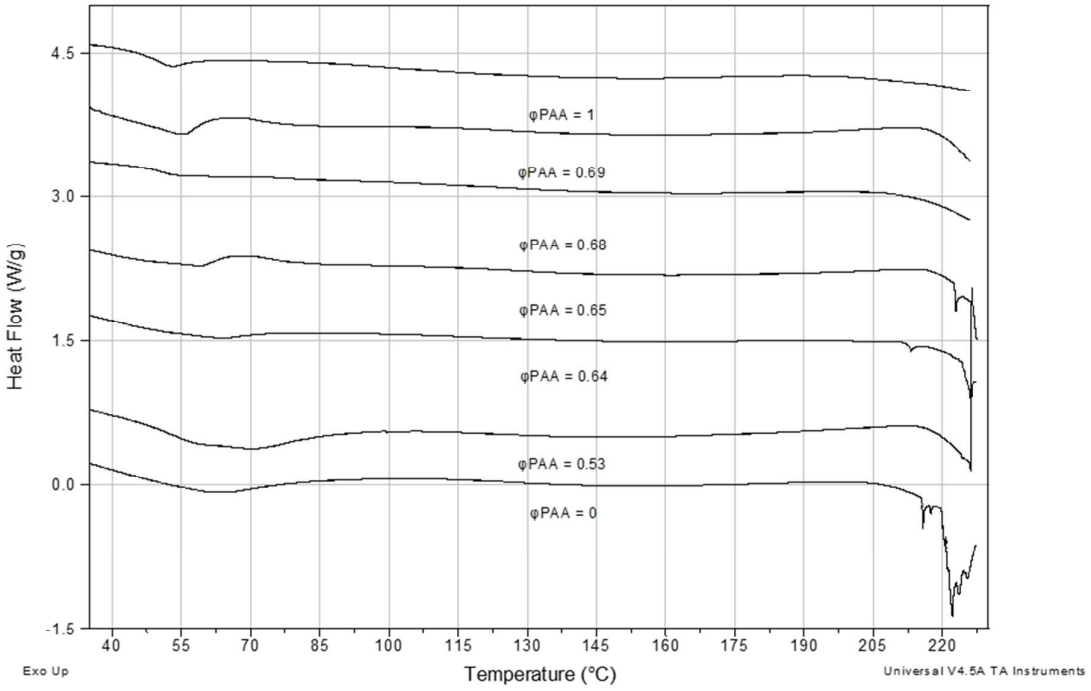

Figure 3. DSC thermograms of IPNs IPN PAAm/PAA with different compositions

In Figure 3, it could be also seen that all IPNs show one very broad glass transition which lies between the T_gs of both SNs PAA and PAAm. The same was observed for the IPNs PAA/PAAm, their thermograms not presented here. One broader T_g region between the *Tg*s of both neat components, i.e. glass-transition temperatures of the two polymers shifting inward, is usually observed in IPNs due to an increase in the miscibility of the two polymers caused by the presence of cross-links [10].

3.4. Calcium phosphates *in situ* formation in IPNs

The *in situ* precipitation of CP into the IPNs was followed gravimetrically. The weight percent of deposited CP into IPNs is shown as a function of the IPNs composition in Figure 4. There is a clear trend of increasing the CPs content as φ^{PAA} increases. This is in line with the recent findings of Yokoi et al that an increase in the number and density of COOH results into a linear increase in the quantity of adsorbed calcium ions [6].

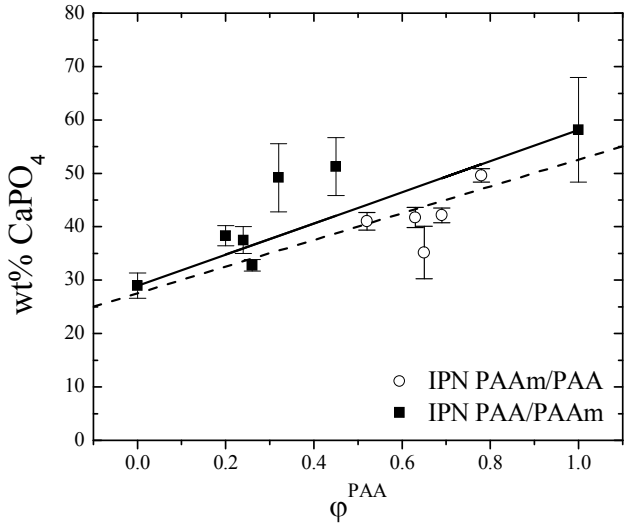

Figure 4. Weight % of CPs *in situ* deposited in IPNs as a function of IPNs composition. Solid line – additivity law, dashed line – linear fit (see text).

In the same study, however, the authors observed the opposite trend concerning the *in situ* deposited CP amount in PAA and PAAm copolymers. Namely, the increase in the COOH groups number resulted into a decrease in the amount of the precipitated CP. This fact was explained by the chelation of calcium ions by the COOH groups which decreased the calcium ions activity and hence the amount of precipitated CP [6].

One should mention here two main differences between our study and the one of Yokoi et al. [6]. Generally we have used (i) much higher (~4 times) concentration of the crosslinking agent which imposed a nano dimension of the phase separated IPN structure (Sheme 1) [11] and (ii) our samples were ~10 times thinner as compared to the used by them. These two factors change the ions diffusion, enhancing it most probably, as compared to the copolymer system studied by Yokoi et al. [6]. As a result, the CP precipitation changed although some their conclusions are valid also for our system. For example, we have also detected the influence of other than the purely concentration dependence of AA content on the CP precipitation. The black line in Figure 4 is drawn according to the additivity law: wt.% $CaPO_4$=29+29.φ^{PAA}. It is seen there that when PAA played the role of a matrix (Scheme 1, IPN PAA/PAAm) the amount of the *in situ* deposited CPs deviates positively from the additivity law (closed symbols in Figure 4), tending towards the amount deposited in the neat PAA. This positive deviation from the additive law means that the CPs deposition is not simply proportional to the acidic groups' concentration in the IPN gels but is *enhanced* due to

other factors. This result is in agreement with the expectations that not only the gel functionality governs the *in situ* CPs deposition in IPNs gels but also their crosslinking density as this is the factor that defines e.g. ions diffusion. Indeed when compare the CP deposition results (Figure 4) with the ESR variation with PAA content one can see that the amount of deposited CP in fact increases with ESR increase (Figure 1), i.e., with the enhancement of the ions diffusion in the IPNs hydrogels (IPN PAA/PAAm, closed symbols in both figures).

In contrast, when PAA played the role of the 2nd network (i.e. nodules were formed from PAA, Scheme 1, IPN PAAm/PAA), the amount of *in situ* deposited CPs in these IPNs deviates negatively, i.e., lower amount of CPs is deposited in the IPN than the predicted from the additivity law. This result also confirms the conclusion that the CP deposition is not simply governed by the acidic functionality availability but also other factors have influence on the process, one possibility being e.g. the changed activity of calcium ions as stated by Yokoi et al. [6].

The amount of the *in situ* deposited CP in the SN PAAm is significantly lower than the amount deposited in the SN PAA which was expected due to the PAA functionality besides the good swelling ability of both SNs. This result was also proved by X-ray measurements (see section 3.9).

The dashed line in Figure 4 is the linear fit drawn according to the experimental points (with error bars as weights). The regression coefficient is 0.908 and the slope is 25±3, which means that both lines – the additivity law and the linear fit in fact coincide within the experimental error.

3.5. Morphology of IPNs with in situ deposited CP

The morphology of broken surfaces of IPN PAA/PAAm (φ^{PAA} = 0.24) and IPN PAAm/PAA (φ^{PAA} = 0.68) containing *in situ* formed CPs were studied by SEM (Figure 5). The morphology of the neat IPNs was already studied in our previous paper [11] and their nano phase separation was detected, the size of the nodules formed from the 2nd polymer network being below 100 nm for all studied IPNs. Coming back to the current study, when PAA formed the matrix and the nodules inside were from PAAm (Scheme 1, IPN PAA/PAAm), the crystallization of CPs depended on the remoteness from the edge of the sample, i.e. from the depth, similarly to the observed by Yokoi et al. for the CP crystallization in neat PAAm gels [5]. At areas close to the sample edge (depth < 30 μm), all studied samples showed small fine crystals from CP formed within the matrix (Figure 5, IPN3). At this depth, the CP

crystals are formed under high supersaturation conditions due to the fact that close to the edge more ions could diffuse into the sample [5]. Under these conditions, the nucleation rate is much higher thus prevailing the process of crystal growth [5]. According to the same authors, these small crystals are further redissolved thus giving rise to larger ones. However, we did not observed it, most probably because we used shorter time for CP maturation - 2 days versus 5 days used in the study of Yokoi et al. [5].

At larger distance from the sample edge (depth > 30 μm) for the same IPNs PAA/PAAm, the observed CP crystals are larger due to the fact that in the core of the sample the ions are in a lower saturation level which promotes the crystal growth rather than the nucleation. This was the case observed for neat PAAm gel with *in situ* deposited CP [5].

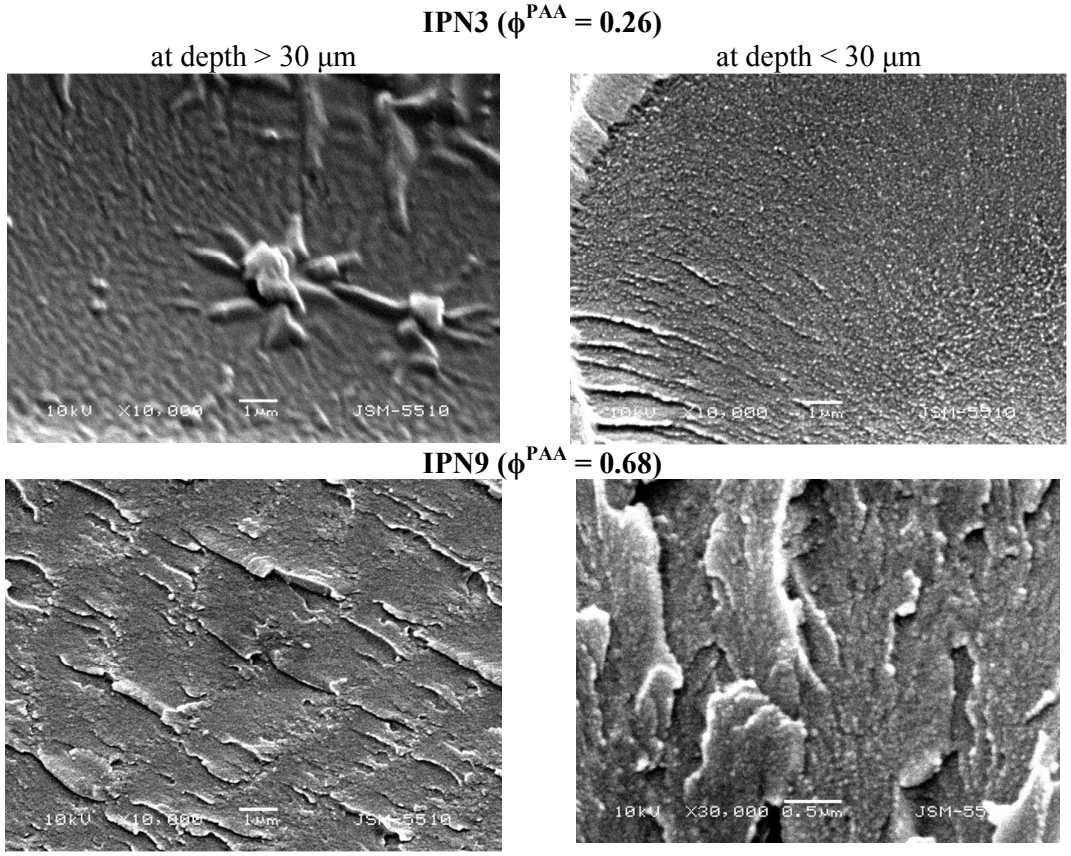

Figure 5. Morphology of broken surfaces of both types IPNs with *in situ* precipitated CP.

When PAAm was the matrix and PAA nodules were dispersed within (Scheme 1, IPN PAAm/PAA), the sample morphology appeared not to depend on the sample thickness and all over the broken surface the small CP grains could be seen (Figure 5, IPN 9). The above mentioned ~4 times higher concentration of the crosslinking agent as compared to the studies

of Ohtsuki group [5, 6] most probably defined the much smaller size of the CP crystals observed for both types of IPNs in the current study.

The small CP grain size, observed for all IPNs samples with *in situ* formed CP, was further proved by TEM, performed on the ashes left after removing the organic part of the sample after heating up to 900^{o}C (Figure S2, Supporting Information). There, the nanometer size of the CP grains could be seen, confirming the small size of the *in situ* formed CP within the IPNs matrices. Thus, the influence of the IPNs network density and structure on the CPs formation, i.e. on biomineralization process was confirmed.

3.6. Thermal properties of IPNs with in situ deposited CPs

The *in situ* CP deposition in the IPNs should affect the latters' thermal properties as it results in the formation of organic-inorganic composite materials. As it could be seen in Figure 6, T_g of the IPNs increases after the *in situ* CP deposition which is in line with the observed T_g increase when inorganic-organic composite material is formed [20]. The T_g increase in organic-inorganic polymer composites is due to the partial immobilization of the polymer chains around the inorganic filler particles. The stronger the interaction between the inorganic particles and the polymer matrix is, the higher is the T_g increase of the composite material. Transferred to the current system, that means that the CP particles interact with the polymer chains in their vicinity thus immobilizing them. As a result, the T_g of the polymer matrix increases. In Figure 5 the thermograms of two IPNs with different compositions are presented without and with *in situ* deposited CPs. For both compositions an increase in the polymer matrix T_g is observed which confirms the assumed interaction between the deposited CPs and the polymer matrices.

The *in situ* deposited CP influence also the IPNs degradation temperatures. As it could be seen in Figure 6, the CP deposition decreases the IPNs' degradation temperature and widens the degradation peak. For comparison, the thermogram of the neat PAAm is presented where the degradation peak around ~220^{o}C is clearly seen. As the amount of deposited CP in the IPNs increases (it increases with φ^{PAA}, as shown in Figure 4), the degradation peak shifts to lower temperatures and becomes wider.

It is shown in literature, that when amorphous calcium phosphates (ACP) and hydroxyapatites (HAP) are deposited in neat PAAm, the PAAm degradation onset is not influenced by the CPs presence [21, 22], i.e., the imidization stage in the PAAm degradation starts as normal at ~220^{o}C. However, for PAA based materials, the presence of HAP causes decrease of the PAA degradation onset [23], which could explain the observed here decrease in the IPNs' degradation temperature and widening of the degradation peak.

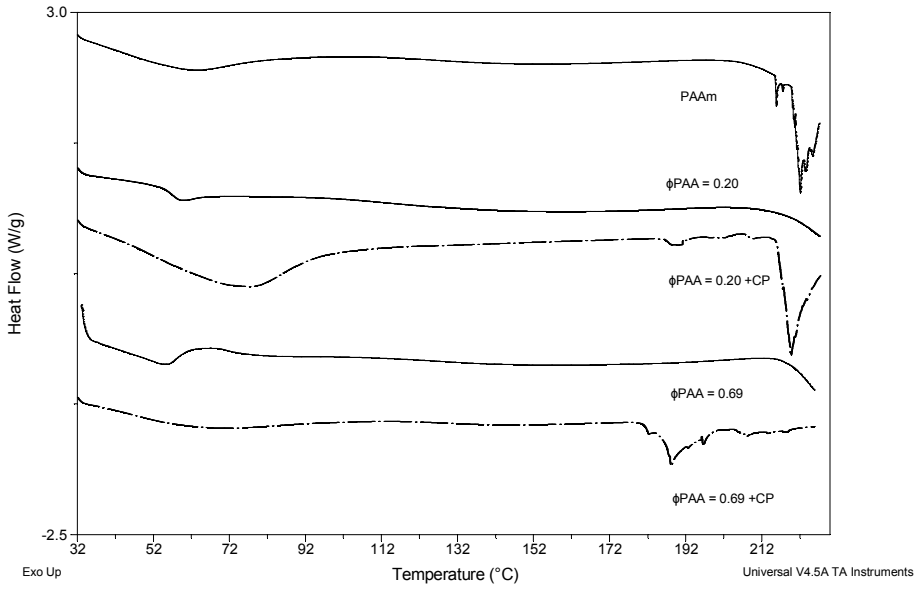

Figure 6. DSC thermograms of IPNs PAAm/PAA with (-·-) and without (—) *in situ* deposited CP. The curves for two IPNs composition designated in the figure are presented

Similar effect on PAA degradation has also $Cu(NO_3)_2$ where as the Cu content increases, the PAA degradation peak shifts from 250 ^oC to almost 150^oC [24]. Thus the presence of CP influences the thermal stability of the IPNs via decreasing the PAA degradation temperature.

3.7. IR characterization of *in situ* deposited CPs into SNs of PAA and PAAm

In Figure 7A, the IR spectra of the neat SN PAAm as well as of the SN PAAm with *in situ* deposited CP (designated as *PAAm+CP*) are presented. Both spectra of SN PAAm and the composite PAAm+CPs are quite similar as they both contain the typical for PAAm bands [24, 25] (see Supporting Information, Tables S1 and S2).

In the *PAAm+CP* the typical amide C=O stretch at ~1655 cm^{-1} is slightly shifted (~1653 cm^{-1}) to lower frequency (resolution of the spectra is ~2 cm^{-1}) which means that this group possibly interacts with the *in situ* deposited CP. The low frequency shift of the C=O stretching vibration in amides was shown to indicate that the C=O bonds in the peptide chain were weakened because of the formation of new chelate bonds between Ca^{2+} and C=O bonds [26].

When comparing *PAAm* and *PAAm+CP* spectra two peaks appear in the latter which are not seen in the former; these are denoted in bold and with asterisk in Figure 7A and are explained in Table 2.

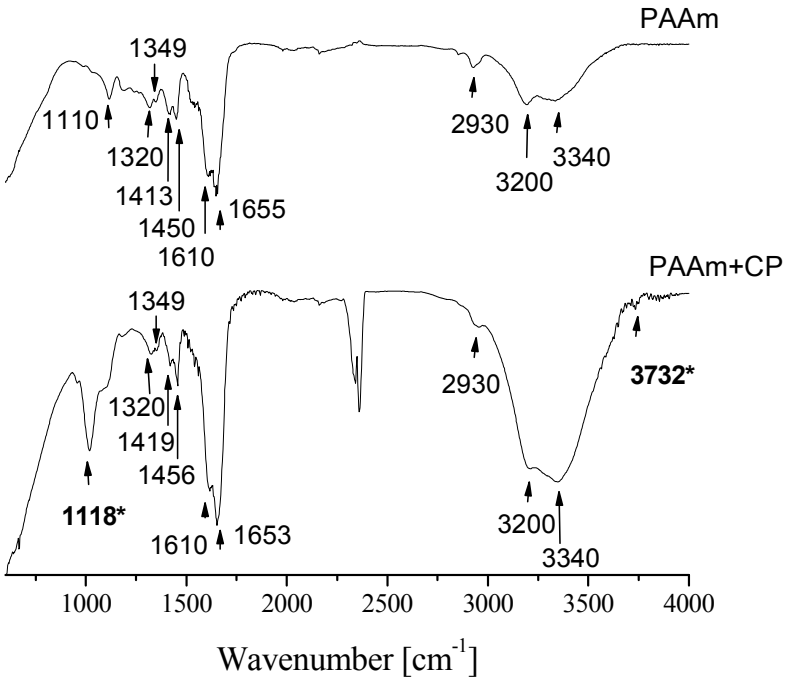

A

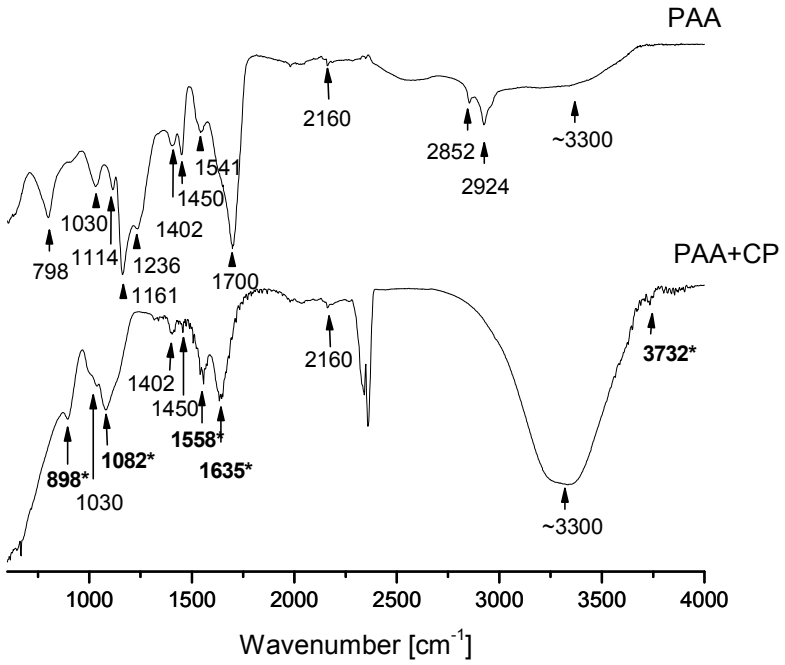

B

Figure 7. AT-FTIR spectra of: (A) neat PAAm and PAAm with *in situ* deposited CP (*PAAm+CP*) and (B) neat PAA and PAA with *in situ* deposited CP (*PAA+CP*).

Table 2. New bands, appearing in the *PAAm+CP* IR spectrum as compared to the neat *PAAm*.

Band position	Attribution	Remark
~1118 cm^{-1}	antisymmetric stretching υ_3^{PO4} in CP	This band usually appears in 900–1200 cm^{-1}, however as the band is neither split nor there is a shoulder, it corresponds to amorphous CP, which coincides with the X-ray data (see section 3.9)
~3732 cm^{-1}	free OH stretching	since this peak does not appear in the neat PAAm spectrum, it originates from the *in situ* deposited CPs

The IR spectra of SN PAA (*PAA*) and PAA with *in situ* deposited CP (designated as *PAA+CP*) again have quite many common bands [24] (see Supporting Information, Table S1). The new bands that appear in the *PAA+CP* sample as compared to the neat *PAA* are in bold and marked with asterisk in Figure 7B and are summarized in Table 3.

Table 3. New bands, appearing in the *PAA+CP* IR spectrum as compared to the neat *PAA*.

Band position	Attribution	Remark

~898 cm^{-1}	P-O-H symmetric stretching mode	this is typical for *acidic CP,* i.e. this is the most characteristic feature of the presence of HPO_4^{2-} species [28]
~1082 cm^{-1}	ν_3^{PO4} stretching	coming from the in situ precipitated CP
~1558 cm^{-1}	asymmetric COO^- stretching ν_{as}^{COO-} of the carboxylic anion [27]	means that COOH groups in *PAA+CP* are transformed into COO-
~1635 cm^{-1}	stretching asymmetric vibration of the carboxylate group in PAA salts [26]	means that COOH groups in *PAA+CP* are transformed into COO- as the stretching of C=O from COOH disappears in the *PAA+CP*
~3732 cm^{-1}	free OH stretching from the *in situ* deposited CPs	Similarly to the case of *PAAm+CP*, as it was explained in Table 2.

The transformation of carboxylic group to carboxylic anion is expected as the carboxylic groups in PAA are assumed to interact with Ca^{2+} and in this way to initiate the CP deposition into the hydrogels. Another proof for this transition is the doublet at 1161 cm^{-1} and 1236 cm^{-1} (for $\upsilon_{C-O} + \delta_{O-H}$) which appears only in the neat *PAA* and disappears in the *PAA+CP* because of the formation of carboxylic anion.

In contrast to *PAAm+CP* spectrum where the band at ~2930 cm^{-1} was assigned to the C-H stretching, in the *PAA+CP* IR spectrum this band is obscured by the broader OH stretching.

In the spectra of *PAAm+CP* and *PAA+CP* two bands appear which are due to CO_2 from air, namely a weak band at 667 cm^{-1} as well as two bands at 2339 cm^{-1} and 2359 cm^{-1} coming from the CO_2 in the beam.

In summary, the CP deposited in both SNs give a typical broad phosphate band due to stretching ν_3^{PO4} modes in the 1000-1100 cm^{-1} region with two distinctive peaks at ~1016 cm^{-1} in *PAAm+CP* spectrum and at ~1082 cm^{-1} in the *PAA+CP* spectrum. Moreover, in the *PAA+CP* IR spectrum the typical band for HPO_4^{2-} groups appears which means that the neat PAA promotes the formation of acidic CPs. In the *PAAm+CP* IR spectrum this band is obscured by the end of the spectrum.

3.8. IR characterization of the *in situ* deposited CP in IPNs of PAA and PAAm

In Figure 8 the IR spectra of *IPNs+CP* (*PAAM+CP* and *PAA+CP*) for several different IPNs' compositions are presented. Several main bands coming from amide or carboxyl groups could be seen there along with the newly appeared bands coming from the in situ formed CP. Table 4 summarizes the new bands in the *IPN+CP* samples coming from the CP or appearing due to the CP formation.

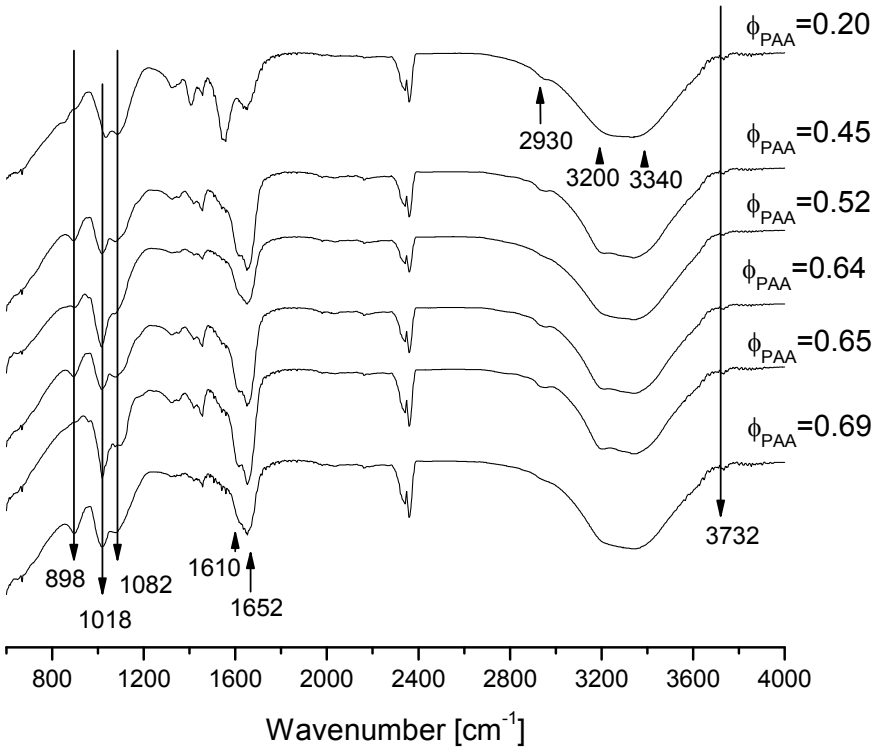

Figure 8. AT-FTIR spectra of IPNs of PAA and PAAm with *in situ* deposited CP.

As the bands due to PO_4 are very broad for all IPNs compositions that means that the precipitated CP in all samples are poorly crystalline which coincides with the results for both SNs with in situ deposited CP: *PAA+CP* and *PAAm+CP*. This data are also confirmed by the X-ray study (see section 3.9).

Table 4. IR bands, newly appearing in the *IPN+CP* IR spectra as compared to the neat PAA and PAAm (data from Figure 8).

Band position	Attribution	Remark
~3000-3600 cm^{-1}	broad band due to the OH stretching from the deposited CPs	appears in all *IPN+CP* samples (designated with a straight line)
~1652 cm^{-1}	C=O stretching vibration in *carboxylic anion*	seen in all samples *IPN+CP* for IPN with φ^{PAA}>0.5
~1016 cm^{-1} and ~1082 cm^{-1}	stretching ν_3PO_4 modes	typical broad phosphate band in the 1000-1200 cm^{-1} region with two distinctive peaks
~898 cm^{-1}	P-O-H symmetric stretching mode	The band was observed in the neat *PAA+CP* and confirms the formation of HPO_4^{2-} groups when *in*

		situ CP were deposited into the IPN hydrogels

3.9. X-ray characterization of *in situ* deposited CPs into SNs and IPNs of PAA and PAAm

In Figure 9 the X-ray diffractograms of three samples – both neat SNs and the IPN5 (φ^{PAA}=0.45) all of them with *in situ* deposited CP are presented. According to the data all samples have relatively low crystallinity which coincides with the broad bands for phosphate group observed by IR. Although the CPs are poorly crystalline, three crystalline phases were identified by the search-match program Match2, namely brushite, sylvite and monetite. A semi-quantitive analysis was performed on the basis of the corundum number and the obtained results are presented in Table 5.

Table 5. Crystalline phases and crystallite size* from the X-ray study on both SNs and IPN5 with *in situ* deposited CPs.

Sample designation	**Brushite** [wt. %] $CaHPO_4 \cdot 2H_2O$ (96-900-7306)**	$D_{<12\bar{1}>}$, [Å]	**Sylvite** [wt. %] KCl (96-900-3130)	**Monetite** [wt. %] $CaHPO_4$ (96-900-7620)	$D_{<\bar{1}03>}$, [Å]
PAAm	-	-	76.6	23.4	360±30
IPN5	69.7	900±27	30.3	-	-
PAA	89.7	340±30	10.3	-	-

* crystallite size $D_{<12\bar{1}>}$and $D_{<\bar{1}03>}$ for brushite and sylvite in direction perpendicular to the $(12\bar{1})$ and $(\bar{1}03)$ plane respectively

** "Crystallography Open Database" # of each phase

In all three samples sylvite (KCl) was identified which is expected as it is the side product of CP deposition. In the neat PAA only brushite was formed most probably due to the acidic environment ensured by the polyanion network (PAA) which promoted the brushite formation. This result coincides with the IR data about HPO_4^{2-} species presence as well as with the COOH transformation to COO^- in the same sample (see Section 3.7).

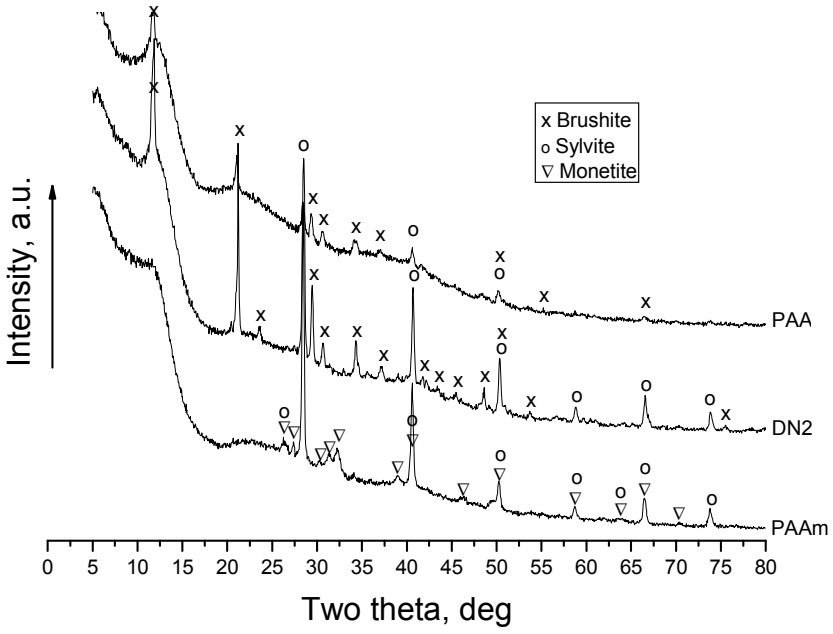

Figure 9. X-ray diffractograms of the materials, obtained after *in situ* deposition of CP into SN PAAm, SN PAAc and IPN5 (φ^{PAA}=0.45)

In the neat PAAm only monetite was formed. After comparison of both diffractograms, it appears that by following the same procedure and solution concentrations for CPs *in situ* deposition, more CPs was deposited in the neat SN PAA than in the neat SN PAAm. This is in agreement with the gravimetrically obtained data about CP deposition in both samples (Figure 4).

In the IPN5 (φ^{PAA}=0.45) only brushite phase of the CP was formed and this could be explained by the PAA leading role in the CP deposition process. This also coincides with the IR data where for all *IPN+CP* materials the band for HPO_4^{2-} appears.

In Table 5 the crystallite size of brushite and monetite in direction, perpendicular to the planes $(12\bar{1})$ and $(\bar{1}03)$, respectively, is also presented. In order to determine them, the $12\bar{1}$ reflections of brushite and $\bar{1}03$ of magnetite were used since these maxima are relatively well expressed. Crystallite sizes in other directions of brushite and monetite in PAA and IPN5 were not calculated due to the lack of appropriate peaks. The crystallite size of sylvite is not discussed as it is a side product and of no interest here.

The size of the brushite crystallites in IPN5 is much higher than that in SN PAA. This could be due to the lower number of acidic groups serving as crystallization nuclei per unit volume

in the former as compared to the latter. As a result, smaller number of crystals with larger sizes are formed in the IPNs as compared to the neat PAA.

The formation of brushite and respectively monetite into the studied SNs and IPNs defines their potential application as bone restoration materials. Brushite and monetite being acidic forms of calcium phosphates are relatively soluble in biological solutions, although in different pH ranges. Brushite when in contact with biological fluids tends to dissolve and re-precipitate into a less soluble calcium phosphate (e.g. hydroxyapatite) [29] while monetite when implanted *in vivo* preserves its chemical composition and degradability, allowing replacement by the newly formed bone tissue [30]. Taking in mind the poor functionality of the damaged tissue surrounding the bone defects, biomaterials based on brushite and monetite are of special interest as they can enhance the process of bone augmentation and restoration.

4. Conclusions

IPNs of PAA and PAAm have been synthesized and characterized in terms of their swelling ability, microhardness and thermal properties. For the first time these IPNs were applied as a polymer template for biomineralization taking advantage of their specific characteristics. Two key factors appear to control the *in situ* CP deposition in the IPNs, namely: the *IPNs' functionality* as well as the *IPNs' hydrogels network density* both controlled through variation of *the IPNs' composition*. Thus the IPNs' potential as a biominerazation template was successfully demonstrated.

Acknowledgements

The work was financially supported by the Bulgarian National Science Fund under Contract DFNI-T02/5.

References

[1] J. D. Addadi, F. Nudelman and S. Weiner, *Chemistry: A European Journal*, 2006, **12**, 980-987

[2] J. D. Kretlow and A. G. Mikos, *Tissue Engineering*, 2007, **13**(5), 927-938

[3] G. Liu, D. Zhao, A. P. Tomsia, A. M. Minor, X. Song and E. Saiz *Journal of American Chemical Society* 2009, **131**, 9937–9939

[4] E. Asenath-Smith, H. Li, C. Keene, Z. W. She and L. A. Estroff, *Advanced Functional Materials,* 2012, **22**, 2891-2914

[5] T. Yokoi, M. Kawashita, K. Kikuta and C. Ohtsuki *Materials Science and Engineering C,* 2010, **30**, 154–159

[6] T. Yokoi, M. Kawashita and C. Ohtsuki *Journal of Asian Ceramic Society* 2013, **1,** 155–162

[7] G. Cama, B. Gharibi, J. C. Knowles, S. Romeed, L. DiSilvio and S. Deb *Journal of The Royal Society Interface* 2014, 11: 20140727

[8] V B. Idowu, G. Cama, S. Deband, L. Di Silvio "In vitro osteoinductive potential of porous monetite for bone tissue engineering" J. Tissue Eng. 5, 1–14 (2014)

[9] T. R. Desai, S. B. Bhaduri and A. Cuneit Tas "A self-setting, monetite ($CaHPO_4$) cement for skeletal repair", Chapter 6 in Advances in Bioceramics and Biocomposites II, Ceramic Engineering and Science Proceedings, Volume 27, Issue 6

[10] Sperling L. H., in: *Interpenetrating polymer networks*, Eds. D. Klempner, L. H. Sperling and, L. A. Utracki, Advances in Chemistry; American Chemical Society: Washington, DC, 1994, p. 24.

[11] M. Simeonov, B. Kostova and E. Vassileva, *Macromolecular Symposia*, 2015, **358**(1), 225–231

[12] M. Muchtardi, J. Levita, D. Rahaya and H. Rahmi, *Food & Public Health*, 2012, **2**(2), 16-20

[13] MATCH!, Version 2.x, CRYSTAL IMPACT, Kreuzherrenstr. 102, 53227 Bonn, Germany, URL http:/www.crystalimpact.com/match

[14] H. P. Klug and L. E. Alexander, *X-ray diffraction procedures for polycrystalline and amorphous materials,* John Wiley & Sons, New York, 1974, p. 511

[15] B. D. Cullity and S. R. Stock, *Elements of x-ray diffraction*, Third Edition, Prentice Hall, New Jersey, 2001, p. 400

[16] M. Edwards, M. M. Benjamin and J. N. Ryan, *Colloids and Surfaces A. Physicochemical and Engineering aspects,* 1996, **107**, 297-307

[17] M. Jiang, M. Li, M. Xiang and H. Zhou, *Advances in Polymer Science*, 1999, **146**, 121-196

[18] F. O. Garces, K. Sivadasan, P. Somasundaran and N. J. Turro, *Macromolecules*, 1994, **7**, 272-278

[19] W. M. Leung, D. E. Axelson and J. D. Van Dyke, *Journal of Polymer Science: Part A: Polymer Chemistry,* 1987, **25**, 1825-1846

[20] D. H. Droste and A. T. Dibenedetto, *Journal of Applied Polymer Science*, 2003, **13**(10), 2149-2168

[21] Q.-L.Tang, K. –W. Wang, Y. –J. Zhu and F. Chen, *Materials Letters*, 2009, **63**(15), 1332-1334

[22] G. S. Sailaja, S. Velayudhan, M. C. Sunny, K. Sreenivasan, H. K. Varma and P. Ramesh, *Journal of Materials Science*, 2003, **38**, 3653-3662

[23] S. Dubinsky, G. S. Grader, G. E. Shter and M. S. Silverstein, *Polymer Degradation and Stability*, 2004, **86**, 171-178

[24] *Infrared spectroscopy of polymers*, Ed. N. A. Del Fanti, Thermo Fisher Scientific Inc., 2008, p. 204

[25] W. Zhang, Z.-L. Huang, S.-S. Liao and F.-Z. Cui, *Journal of the American Ceramic Society,* 2003, **86,** 1052-54

[26] B. Grabowska, M. Sitarz, E. Olejnik, K. Kaczmarska and B. Tyliszczak, *Spectrochimica Acta, Part A: Molecular and Biomolecular Spectroscopy,* 2015*,* **151**, 27-33

[27] M. B. Povea, W. A. Monal, J. V. C. Rodríguez, A. M. Pat, N. B. Rivero and C. P. Covas C. P., *Materials Sciences and Applications*, 2011, **2**, 509-520

[28] C. Holt C., M. J. J. M. Van Kemenade, J. E. Harries, L. S. Nelson, R. T. Bailey, D. W. L. Hukins, S. S. Hasnain and P. L. De Bruyn, *Journal of Crystal Growth*, 1988, **92**, 239-252

[29] M. Kumar, J. Xie, K. Chittur and C. Riley *Biomaterials* 1999, **20**, 1389-1399

[30] B. Idowu, G. Cama, S. Deband and L. Di Silvio *Journal of Tissue Engineering* 2014, **5**, 1–14